Pacific Northwest
NATIONAL LABORATORY

PNNL-29326

PIE of Cycle 13 316SS Cladding Using Aberration Corrected STEM Image and Analysis

September 2019

Dan J. Edwards
Matt Olszta
Dion Sunderland
Arun Devaraj
Shenyang Hu
Alan Schemer-Kohrn
Bethany Matthews

U.S. DEPARTMENT OF ENERGY

Prepared for the U.S. Department of Energy
under Contract DE-AC05-76RL01830

DISCLAIMER

This report was prepared as an account of work sponsored by an agency of the United States Government. Neither the United States Government nor any agency thereof, nor Battelle Memorial Institute, nor any of their employees, **makes any warranty, express or implied, or assumes any legal liability or responsibility for the accuracy, completeness, or usefulness of any information, apparatus, product, or process disclosed, or represents that its use would not infringe privately owned rights**. Reference herein to any specific commercial product, process, or service by trade name, trademark, manufacturer, or otherwise does not necessarily constitute or imply its endorsement, recommendation, or favoring by the United States Government or any agency thereof, or Battelle Memorial Institute. The views and opinions of authors expressed herein do not necessarily state or reflect those of the United States Government or any agency thereof.

PACIFIC NORTHWEST NATIONAL LABORATORY
operated by
BATTELLE
for the
UNITED STATES DEPARTMENT OF ENERGY
under Contract DE-AC05-76RL01830

Printed in the United States of America

Available to DOE and DOE contractors from the Office of Scientific and Technical Information,
P.O. Box 62, Oak Ridge, TN 37831-0062
www.osti.gov
ph: (865) 576-8401
fax: (865) 576-5728
email: reports@osti.gov

Available to the public from the National Technical Information Service
5301 Shawnee Rd., Alexandria, VA 22312
ph: (800) 553-NTIS (6847)
or (703) 605-6000
email: info@ntis.gov
Online ordering: http://www.ntis.gov

PNNL-29326

PIE of Cycle 13 316SS Cladding Using Aberration Corrected STEM Image and Analysis

September 2019

Dan J. Edwards
Matt Olszta
Dion Sunderland
Arun Devaraj
Shenyang Hu
Alan Schemer-Kohrn
Bethany Matthews

Prepared for
the U.S. Department of Energy
under Contract DE-AC05-76RL01830

Pacific Northwest National Laboratory
Richland, Washington 99354

Summary

Microstructural analyses were performed on archive materials and irradiated 316SS cladding from the Cycle 13 TPBAR. Optical, SEM, and TEM analysis confirmed the presence of moderate sensitization in the 20% cold worked 316SS after the iron aluminide coating was applied. The Cr depletion occurs on the grain boundaries between the closely spaced carbides, and at the interface between the carbides and matrix. Cr depletion averaged 15 wt% on the grain boundaries and carbide interfaces, but a few isolated regions had depletion levels down to 12.5 wt%. Microscopy analyses were performed on a weld heat affected zone (HAZ) region after an end plug cap had been welded to the coated cladding. Optical and SEM images taken from a weld heat affected zone revealed certain locations near the weld reached temperatures high enough to produce recrystallization, removing the cold worked structure and producing an equiaxed grain structure through much of the HAZ. The high temperatures in this recrystallized region of the HAZ resolutionized the carbides, which was confirmed by subsequent TEM/STEM analysis of a FIB lamella extracted from this region. Not only was the Cr depletion completely removed, it was replaced by a slight enrichment of Cr and Mo.

Three locations were examined with TEM/STEM in the Cycle 13 TPBAR. The locations corresponded to small but important changes in irradiation temperature and dose: Upper End (320-330°C, 5.5 dpa), Mid-plane region (~315°C, 5.5 dpa) and Lower End (~300°C, 4.7 dpa). Vacancy cluster stability begins to decrease when the irradiation temperature reaches ~320°C, allowing the onset of void swelling; at temperatures lower than 320°C only bubbles are seen, rarely voids. Irradiation of the coated cladding produced some surprising changes to the microstructure when compared to results obtained for other light water and fast reactor irradiated 304 and 316SS. The first observation was the restructuring of the cold worked dislocation structure into a mix of line dislocation segments and loops, which clustered together to form an ill-defined, pseudo-cellular structure with cell interiors relatively free of defects. Additionally, neutron irradiation produced a high degree of Ni and Si radiation-induced segregation (RIS) to the line dislocation segments and formed precipitates in the matrix and on grain boundaries. The Ni/Si ratios measured on the line dislocations, grain boundaries, and on discrete precipitates proved to be similar, matching that of the γ′ Ni_3Si phase. This was confirmed by dark field imaging using a precipitate reflection in the diffraction pattern that corresponds to γ′. In the lower end sample, direct evidence of γ′ precipitation was observed on both matrix dislocations and dislocations within a grain boundary that happened to be inclined in the foil, thereby allowing direct observation of the precipitates using dark field imaging. The RIS of Ni and Si to the grain boundaries also depleted the Cr from the boundaries. The broad (±250 nm) Cr depletion profile produced by sensitization was effectively removed and replaced by a much narrower and more severely depleted Cr profile (±10 nm) with minimum Cr levels of 8 wt% or more. This change in the Cr profile during irradiation was accompanied by enrichment of the Ni to levels of ~40 wt% and the Si to ~12 wt%, levels not observed in any other LWR irradiated stainless steel the author has characterized.

With respect to the susceptibility to stress corrosion cracking and irradiation-assisted stress corrosion cracking of this coated cladding, it is worth noting that over 6500 TPBARs have been irradiated without any known incidences of cracking. This is likely due to the combination of the low corrosion potential in the PWR water and to a low stress in the cladding. With respect to stresses, it is assumed by the authors that as the TPBARs are removed from reactor and placed in a spent fuel pool, the internal gas pressure from the helium decreases quickly as the temperature decreases, hence removing the stress during storage in the pool. During service, the only issue that might warrant concern is if there are regions within the assembly where the

irradiation temperature and dose are high enough to promote enough void swelling that creates unexpected stresses due to unrelieved volume expansion. The HAZ of the end plug has a much different microstructure than the rest of the TPBAR cladding, so how it evolves under temperature may be different than the more highly cold worked and sensitized cladding. Residual stresses around the HAZs in welded core components have been areas that have seen cracking failures in LWRs, so it may be worthwhile to perform PIE on those regions if the irradiation temperature and dose are high enough.

Acknowledgments

The authors would like to acknowledge the help of the TTP Science program for the opportunity to perform this work. We gratefully acknowledge the guidance of Dave Senor in this work, and the help of Gary Sevigny.

Acronyms and Abbreviations

BF – Bright Field
CDF – Centered Dark Field
DIC – Differential Interference Contrast
EDS – Energy Dispersive Spectroscopy
FIB – Focused Ion Beam
HAZ – Heat Affected Zone
HAADF – High Angle Annular Dark Field
LWR - Light Water Reactor
PWR – Pressurized Water Reactor
RIS – Radiation-Induced Segregation
STEM – Scanning Transmission Electron Microscopy
SEM – Scanning Electron Microscopy
STEM – Scanning Transmission Electron Microscopy
TEM – Transmission Electron Microscopy
TPBAR – Tritium Producing Burnable Absorber Rod
WBDF – Weak Beam Dark Field

Contents

Figures

Tables

1.0 Introduction

The TMIST-2 experiment noted a radiation enhancement in tritium permeation through the 20% cold worked 316SS cladding used in TPBARs. The mechanism for the radiation enhancement in permeation is not currently understood. If the source of this enhanced permeation resides in the microstructural state before or after irradiation, then it is important to characterize the microstructure across the cladding wall to document these features and any radiation-induced changes that might have led to the enhanced permeation. This characterization should include the aluminide coating and adjacent base metal, which is fairly unique to the TPBARs and has no corresponding dataset in the LWR industry. For example, it has long been known that the 316SS was sensitized during the aluminide coating treatment, but no experimental characterization of the extent of sensitization has been previously performed. Nor is it known if the aluminum has diffused into the underlying steel due to irradiation-induced ballistic injection and enhanced diffusion. The possibility of sensitization has led to a conservative approach on how these components are stored to ensure no potential for failure, so confirmation of the degree of sensitization could help to remove some of the constraints for handling the cladding tubes.

Decades of work on light water reactor (both in-core and out of core) and fast reactor irradiated stainless steels has produced enough data to allow us to predict the basics of the microstructural evolution, but the details are always subject to variability due to differences in thermomechanical processing of the components, differences in alloy chemistry, and the operating parameters of the reactor. In this case, the TPBARs experience a change in internal pressure over the lifetime of the TPBAR. The presence of helium produced by neutron reactions can produce embrittlement by migrating to grain boundaries and promote helium bubble nucleation. An additional factor is that the irradiation temperatures vary along the length of the TPBAR, ranging from 290ºC near the bottom to ~330ºC near the top end of the TPBAR. This higher temperature is of particular concern because it places the 316SS cladding in the void swelling regime, which can be kicked off at a lower incubation period in the presence of helium since helium bubbles act at the nuclei for void formation. The bottom line is that to understand how the 316SS is behaving requires a careful evaluation of dislocation structures, microchemical changes, and possible bubble and/or void formation in the cladding.

New tools have become available in recent years that allow the microstructure to be probed in greater detail than ever before. These tools include the new aberration corrected transmission electron microscopes (AC-TEM) and 3D-atom probe tomography (3D-APT), which when used together can create a framework of the microstructural evolution over a broad scale, from the millimeter to the atomic scale. In this proposal, post-irradiation examination will be performed on Cycle 13 cladding using aberration corrected scanning transmission electron microscopy. A separate proposal will utilize 3D-APT to analyze samples taken from the same regions used for this study; those results will be presented separately.

2.0 Experimental Approach

Characterization was performed on both archive cladding material and on samples extracted from one of the Cycle 13 lead use TPBARs to enable a comparison on the effect of neutron irradiation on the microstructure. The archive materials included coated cladding for C13 obtained from the SALK facility and a separate (representative non-C13) sample from a weld HAZ from a piece of coated cladding to which an end plug was welded. Optical and SEM images were taken of the archive materials to establish the degree of sensitization from the coating process and how this was affected by welding. For the irradiated cladding, metallography samples were provided by the TTP program from three different positions to span the dose and temperature range within the TPBAR assembly. The nominal irradiation conditions for these three locations are listed in Table 1, and specified composition of the cladding is provided in Table 2.

Using the Helios FIB/SEM in RPL, TEM lamella were milled from the center of a mounted cross-section used for the optical and SEM of the unirradiated cladding, with the understanding that the thin walled tubes would experience the same thermal history through thickness. Additional lamellae were prepared to explore the effect of welding on the sensitization. For the irradiated Cycle 13 TPBAR, TEM samples were extracted from the middle of the mounted cross-sections prepared from the three different locations listed in Table 2. In the midplane regions only, additional samples were taken near the outer wall of the tube (waterside), and from the interface between the Fe-Al coating and cladding. These samples were transported to 3410 and given a final thinning to ~250 nm, leaving a U-shaped rim around the edges of the sample that provides support to keep it from bending from residual stresses. After the final thinning in the FIB, flash electropolishing was used to reduce the sample to its final state, a step introduced recently to remove the artifacts from the Ga ion damage when milling TEM lamella.

Table 1. Location of Cross-Sections and Irradiation Conditions

Location Along TPBAR	ID Code	Dose (dpa)	Irradiation Temperature °C	Location of FIB Samples in Cross-Section Sample
Upper End	C13-2-5-4	~5.5	320-330°C	Water Side
Mid Plane	None provided	~5.5	315°C	Water Side Middle of cladding width Coated Interface
Lower End	C13-2-1-1	~4.7	300°C	Water Side

Table 2. Specified Composition

	C	Mn	S	P	Si	Ni	Cr	Mo	N	Co
Specification Range	0.05 - 0.061	1.53 – 1.72	0.003 – 0.006	0.005 – 0.016	0.053 – 0.072	13.14 – 13.74	17.24 – 17.97	2.21 – 2.49	0.005 – 0.0072	0.008 – 0.027

The FIB damage to which we are referring is presented in **Figure 1**, showing that the Ga ion beam yields both “black spot” damage, as well as a “reconstructed” surface layer that obscures the radiation damage present at lower irradiation temperatures. The reconstructed surface layer reveals itself as moiré fringes over the entire lamella when it is imaged in a strong diffraction condition, which is responsible for the muddied contrast in the image from the FIB milled HT9 sample. Flash electropolishing is a controlled microsecond electropolish process that we have developed internally in our group. The details of this were recently reported by Schemer-Kohrn et al [1], and have proven successful on a wide range of Fe-based alloys such as austenitic stainless steels, dual phase cast stainless steels, and various ferritic alloys.

The microstructural analysis was performed on the JEOL 200ARMCF located in the 3410 building. This instrument is a cold field emission, aberration corrected STEM/TEM operating at 200 keV, and is configured with the latest energy dispersive spectrometer (EDS) and a separate electron energy loss spectrometer (EELS), as well as STEM bright field and high angle annular dark field (HAADF) detectors. The microstructural analysis will focus on measuring the defect structure (network dislocation density and/or faulted Frank loops) to obtain their size and density within both the unirradiated and the irradiated samples, and checking for any voids or bubbles that may have formed in the irradiated cladding. Frank loops are faulted defects that can be imaged directly by selecting the diffraction streak (illustrated in **Figure 2**) caused by the stacking fault in the loop, allowing an unambiguous method to image the loops. This method was used quite extensively in prior work by one of the authors [2]. Grain boundary sensitization will be probed using high resolution elemental mapping on both the unirradiated archive and the irradiated materials. The probe in STEM mode is aberration corrected, and for the parameters chosen in this study yielded a high current density probe (~1 nA) with an approximate diameter of ~0.18 nm. To probe the very fine radiation-induced segregation (RIS) profiles, step spacings of 0.13 nm were used with drift correction. Precipitate phases that may have formed during thermomechaical processing and/or during irradiation were documented by elemental mapping, electron diffraction, and high resolution imaging. Voids and bubbles were imaged through focal imaging in conventional TEM mode.

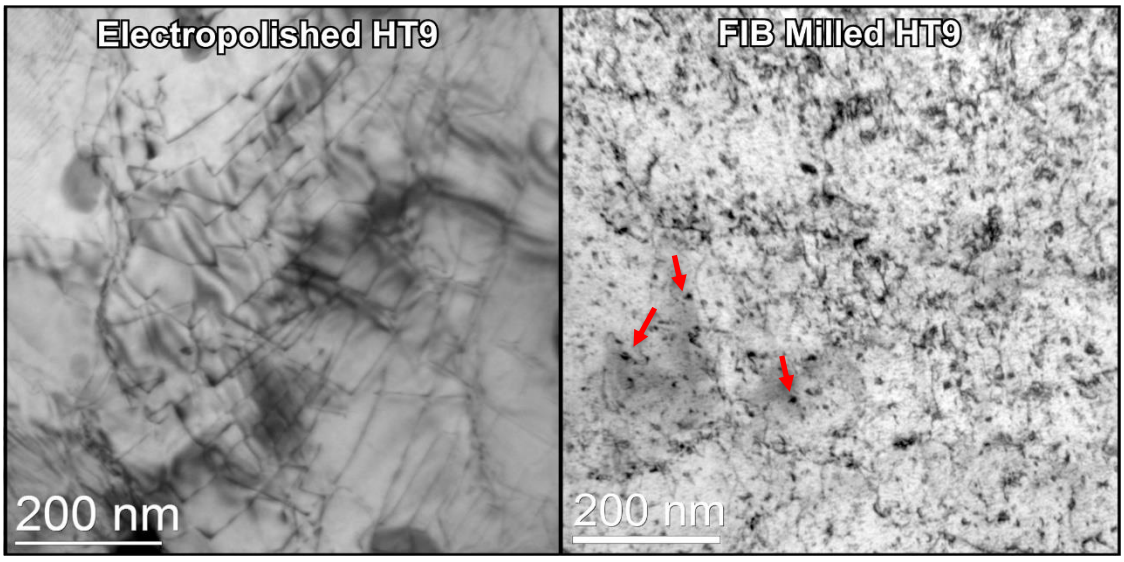

Figure 1. Comparison of a TEM bright field image from an electropolished TEM disc of unirradiated HT9, an Fe-12Cr ferritic steel, with a FIB liftout from the same material. While the line dislocations are the same in each sample, the numerous black spots (red arrows) in the FIB lamella are Ga beam artefacts.

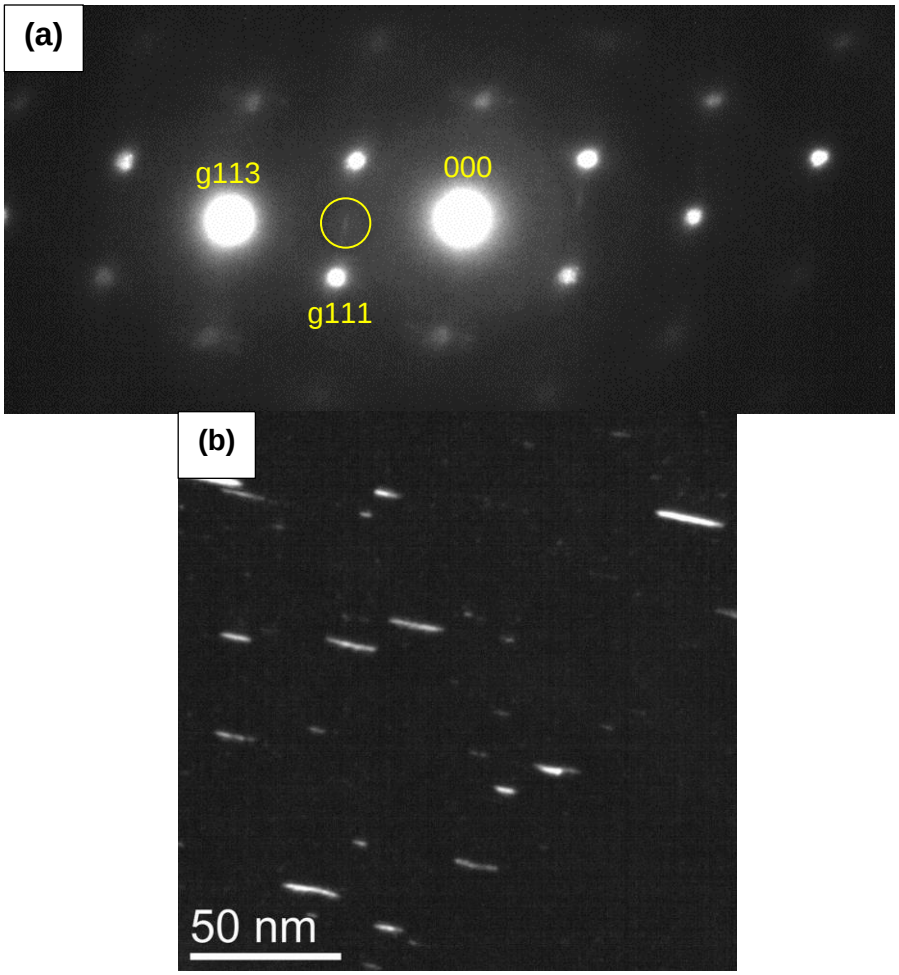

Figure 2. (a) provides an example of diffraction pattern showing the reciprocal lattice streaking due to the high density of faulted Frank loops. The sample is tilted to create a 2-beam condition with the **g**113 lattice spot, which allows one variant of the edge-on Frank loops to be imaged with the encircled streak shown in diffraction pattern. The Frank loops imaged with the streak are shown in (b). Note the streak is perpendicular to the edge-on loop.

3.0 Results

3.1 Optical and SEM of Coated Archive with Weld HAZ

Limited optical results are available for a sample of the coated tube with an end plug cap welded to the thin walled coated tube. Though not Cycle 13 archive material, the sample is representative of what the coating treatment does to the TPBAR tubing microstructure, highlighting the carbide distribution and grain structure of the tube and what effect welding has on the sensitization. **Figure 3** shows a differential interference contrast (DIC) image of the polished cross-section of the thin walled tube with Fe-Al coating on the right side. The grain boundaries and deformation twins are easily distinguished by selective etching from the slightly caustic colloidal silica final polish. The SEM images in **Figure 4** show more clearly the fine, semi-discontinuous carbides decorating the grain boundaries, which are a direct result of the sensitization that pulls Cr from the boundaries and forms carbides, making them susceptible to etching by the colloidal silica. The SEM images don't necessarily indicate etching of the boundary itself, but more relief etching of the carbides. This grain boundary grooving disappears as you move into the weld HAZ, which arises because the carbides have been dissolved and the Cr and C placed back into solution. The SEM images in **Figure 5** show the recrystallized grain structure, lack of carbides, and the subsequent lack of grooving with the Cr depletion removed by the welding temperature exposure.

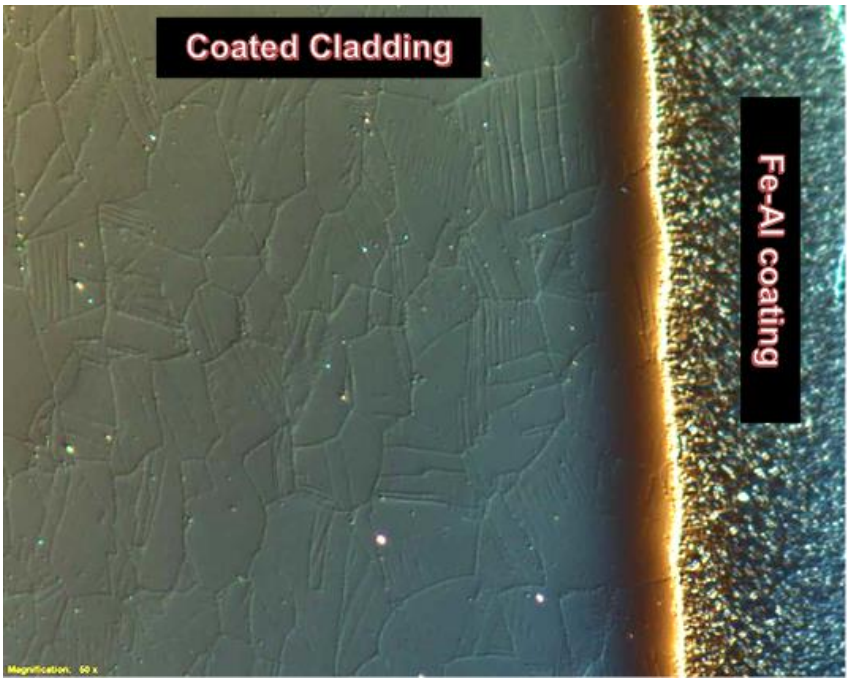

Figure 3. DIC imaging shows the grain boundaries by virtue of the relief etching that occurs under the final colloidal silica polish. The etching arises due to the sensitization present in the cladding, which produced fine carbides. The carbides aren't easy to see in the optical images, however, SEM and TEM clearly show their presence.

Figure 4. The yellow arrows point to fine carbides located on each grain boundary in the coated cladding welded to the end plug cap. The bright spots (red arrow) are colloidal silica particles that didn't rinse off.

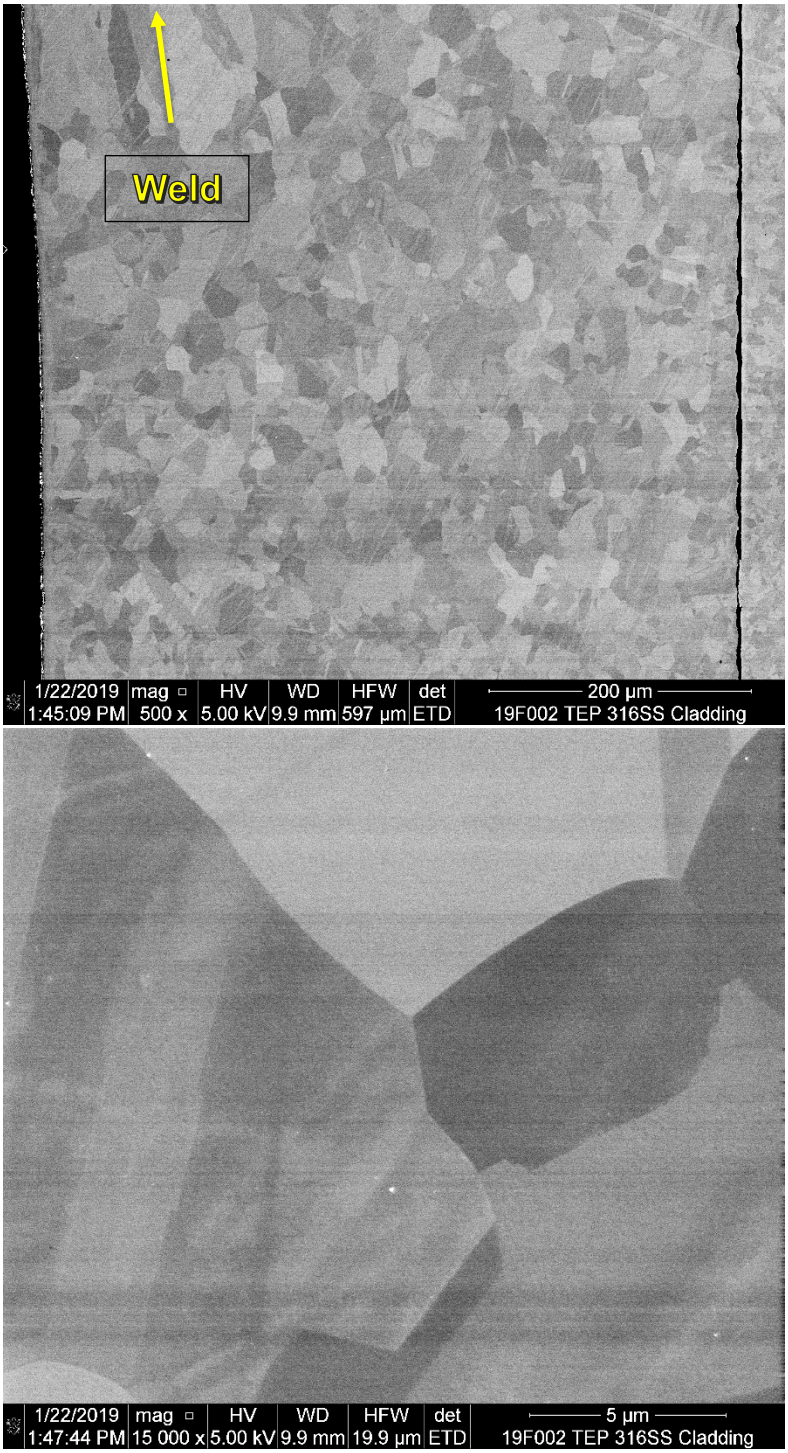

Figure 5. Secondary electron images reveal in the HAZ that the thermal transients lead to recrystallization of the cold worked tube and dissolved the carbides.

3.2 TEM Results

3.2.1 Unirradiated Coated Cladding

The coated cladding exhibits a high dislocation density with multiple deformation twins and deformation bands, examples of which are shown in **Figure 6**. The line dislocation density near the edge of the TEM lamella was found to be ~10^{15} per m^2, near the limit of being able to measure accurately with TEM. The yellow arrows in **Figure 6** point to the twin and grain boundary regions that are common to each of the images (Note that the image in 6(b) is rotated from the STEM images in 6(c) through 6(e). Fine carbides are distributed on both grain boundaries and incoherent twin interfaces, the latter of which were induced by the heavy cold work prior to coating. Edge-on boundaries exhibit closely spaced carbides that are difficult to resolve individually except in the thin regions. By comparison, the inclined grain boundary in **Figure 6(e)** shows more clearly the discrete carbide particles, which are often faceted, triangular shaped particles. A rough size estimate places the carbides ~100 nm in longest dimension. The elemental map shown in **Figure 7** paints a clear picture of the extent of carbide precipitation in this heavily deformed microstructure. There was no suggestion of any carbide precipitation in the matrix.

To quantitively assess the extent of Cr-depletion at the sensitized grain boundaries, full resolution profiles (0.13 nm pixel spacing) were extracted from the elemental maps. **Figure 8** presents the profiles obtained from across the carbides and at locations between carbides, which is somewhat difficult given their close spacing. Bruemmer et al [3] indicated that 316SS becomes susceptible to stress corrosion cracking when the Cr-depletion levels reach a threshold of 12.5 to 13.5%, dependent of course on the corrosion potential, water chemistry, and stress state. The profiles show in **Figure 8** reveal that Cr depletion, though variable from location to location, reached this threshold on the interface between the carbide/matrix interface and in grain boundaries between carbides. The profile width approaches ±250 nm on either side of the boundary or carbide.

To assess the effect of welding upon the sensitized microstructure, a FIB lamella was taken from within the HAZ where the grain structure had clearly been recrystallized based upon optical and SEM images. The set of figures in **Figure 9** reveals clean grain boundaries, with no hint of carbide precipitation and very few dislocations, indicating the Cr and carbon were placed back into solution. Careful examination of the grain boundary chemistry revealed that thermal nonequilibrium segregation (TNES) [4] had occurred during the welding, resulting in both Cr and Mo being enriched by a couple of wt% each to the grain boundary, which has a minor beneficial effect of delaying radiation-induced depletion of Cr.

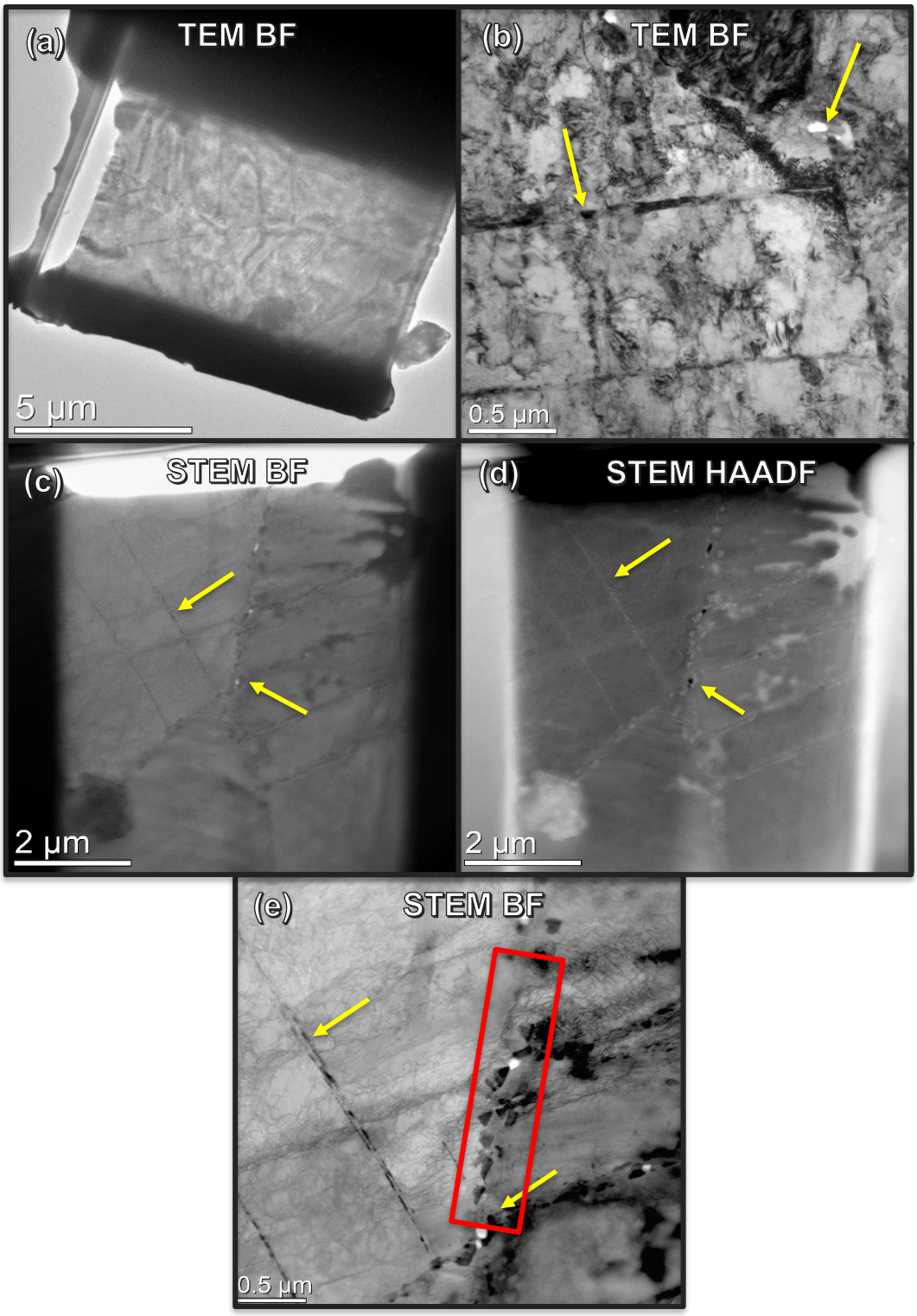

Figure 6. TEM and STEM of coated 316SS archive: (a) an overview after FEP, (b) TEM bright field of the highly cold worked dislocation structure and twins, (c) and (d) are STEM HAADF and BF images, respectively, and (e) is a STEM showing the dense dislocation structure and carbides on a highly inclined grain boundary (red box). Yellow arrows refer to the same features in each micrograph.

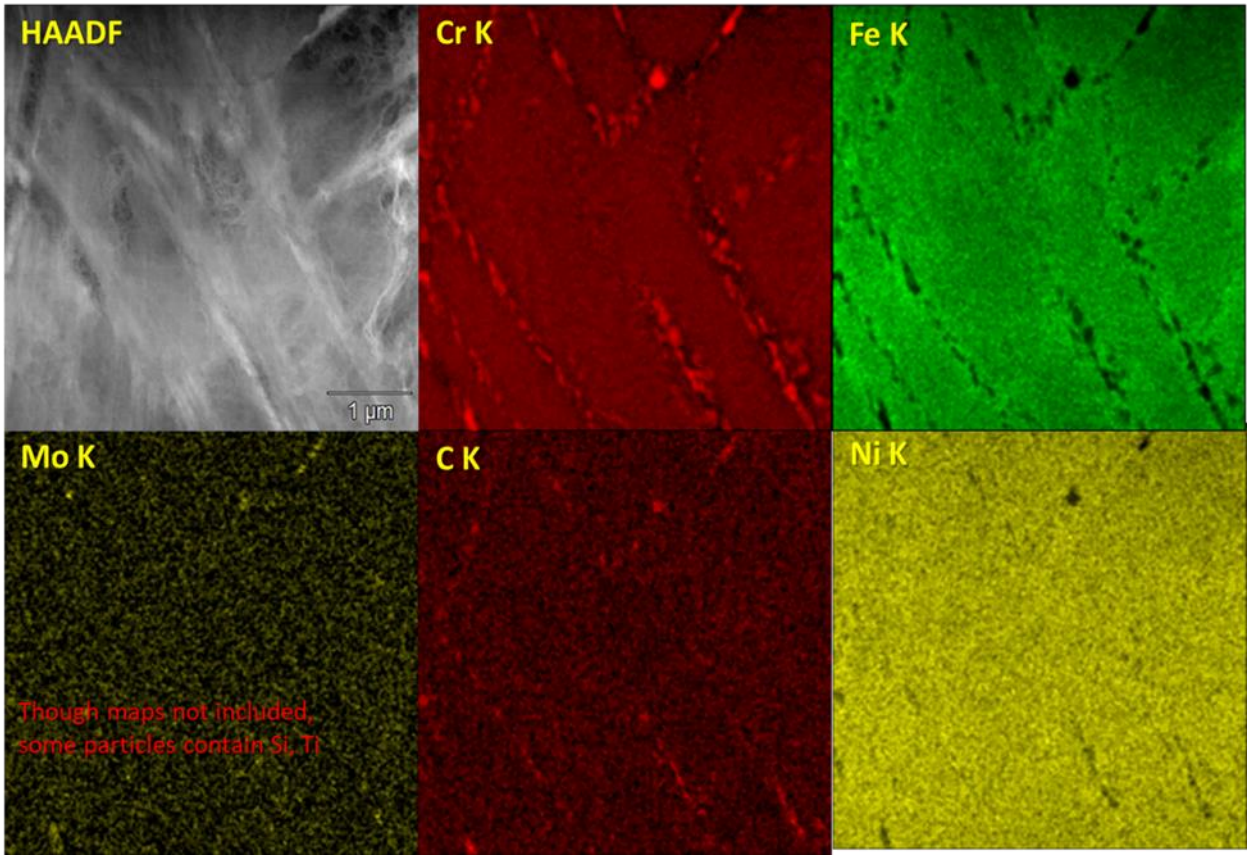

Figure 7. Elemental maps with a high current density probe, revealing the extensive carbide precipitation present throughout the sample. Note the carbon map is less reliable than the Cr map due to the absorption of the low energy C Kα x-ray (0.277 eV). The Cr depletion is primarily offset by Fe enrichment.

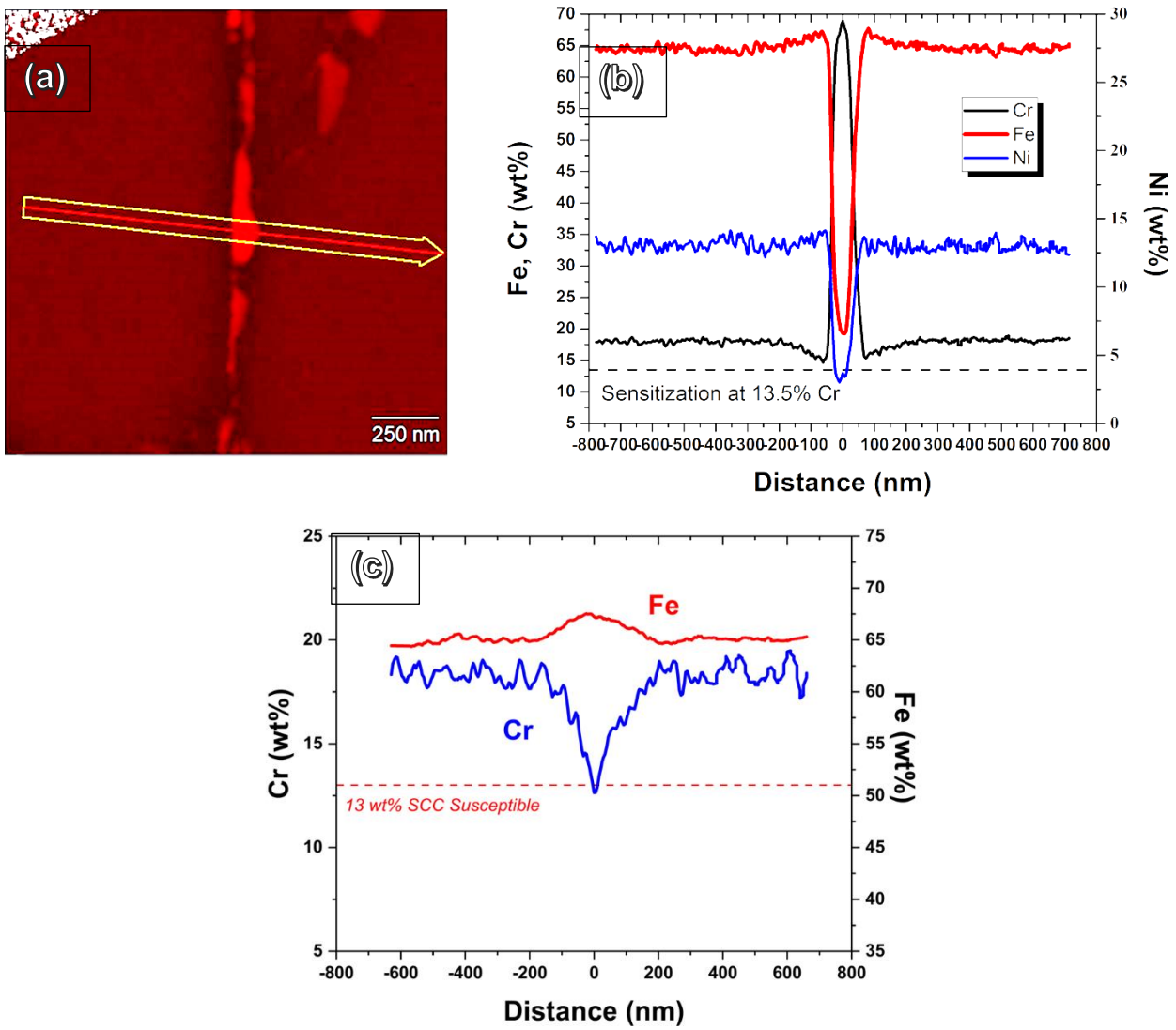

Figure 8. The STEM image in (a) shows a grain boundary near the edge of the FIB lamella which was mapped. The two sets of elemental profiles in (b) and (c) show the maximum Cr-depletion found in this condition (b) adjacent to a carbide and (c) on the grain boundary between carbides. In both cases the Cr-depletion reaches a level below 13.5 wt% Cr.

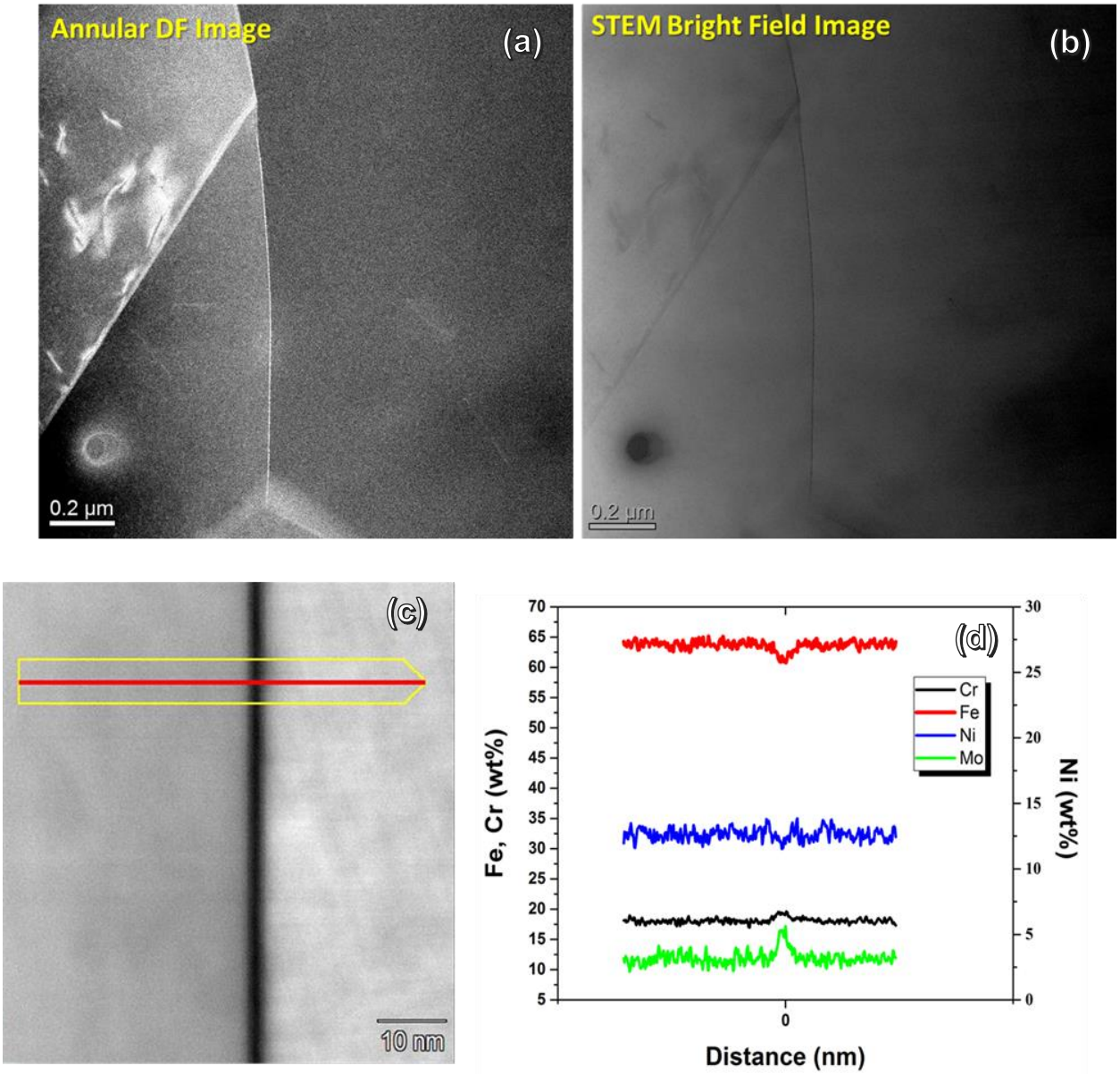

Figure 9. Recrystallized grain structure in the HAZ was found to possess no carbides, and the Cr and Mo were actually enriched by a couple of wt% due to thermal non-equilibrium segregation.

3.2.2 Upper End of Cycle 13 TPBAR

A FIB sample was extracted from the center of the metallography sample (C13-2-5-4) and transferred to 3410 for final thinning using both FIB and flash electropolishing. An overview of the FIB lamella is shown in **Figure 10**, along with TEM and STEM bright field images taken near a 110 zone axis. The line dislocation density is still similar overall of that of the unirradiated archives (~1 x 10^{15} m^{-2}), but considerable restructuring of the cold worked dislocations has occurred. The network dislocations have been replaced by more discrete dislocation segments and loops, with clustering of the dislocations into more localized tangles or cell walls, with regions in between that are relatively free of dislocations. This particular FIB lamella did not have any high angle grain boundaries, so the focus was on the dislocation, precipitate, and void evolution. Images of the defect structures in the upper cladding are presented in **Figure 11**. A high density of Frank loops was observed throughout the foil, but because of foil bending, it wasn't clear how uniform this distribution was in light of the clustering found to occur in the previous image. While the larger loops are easily visible in centered dark field by using the reciprocal lattice streak formed in the diffraction pattern by the fault plane of the loops, there are many smaller defects that are simply bright dots. These small features aren't easily discernible in the bright field images, so it isn't clear if these are very small Frank loops or some other defect such as a stacking fault tetrahedra. Higher magnification images didn't resolve this any further. γ′ precipitation is present throughout the foil, but it wasn't clear if this formed on the small loops as there was rarely a direct association between loop and precipitate. Finally, it was observed that small voids (no visible bubbles) have formed at this dose. Though the total swelling is less than 0.1%, void density is nearly ~1 x 10^{22} m^{-3} and the average size is ~4 nm, indicating that at the higher temperature of the TPBAR assembly, void swelling is beginning. The void swelling is likely kicked off by the helium produced during irradiation, either from decay of tritium or directly from any transmutation reactions in the cladding. Elemental mapping of the matrix revealed that Ni and Si have segregated to line dislocations, and have formed small Ni-Si rich clusters in the matrix with a Ni/Si ratio of 3 to 1, essentially γ′. **Figure 12** shows an example of the Ni and Si precipitation and segregation in the matrix. This is one of the first studies that the authors are aware of documenting γ′ precipitation in the matrix and Ni/Si enrichment to dislocations by EDS elemental mapping, usually this can only be accomplished by 3D-atom probe tomography. Note that the Ni/Si enrichment is accompanied by a depletion in both Fe and Cr.

Figure 13 and **Table 3** present a summary of the loop, precipitate and void statistics for each of the 3 locations within the TPBAR assembly. The average size of the loops is fairly similar; however, it is worth noting that in the upper location the loop distribution exhibits a broader distribution. In contrast, at the midplane and lower position the distribution is definitively asymmetric, with a peak around 2.5 to 3.5 nm and a tail that extends up to 30 nm. The precipitation is less temperature sensitive, with perhaps a slightly smaller average size in the upper region, but still fairly Gaussian in all three locations. The void distribution is fairly Gaussian.

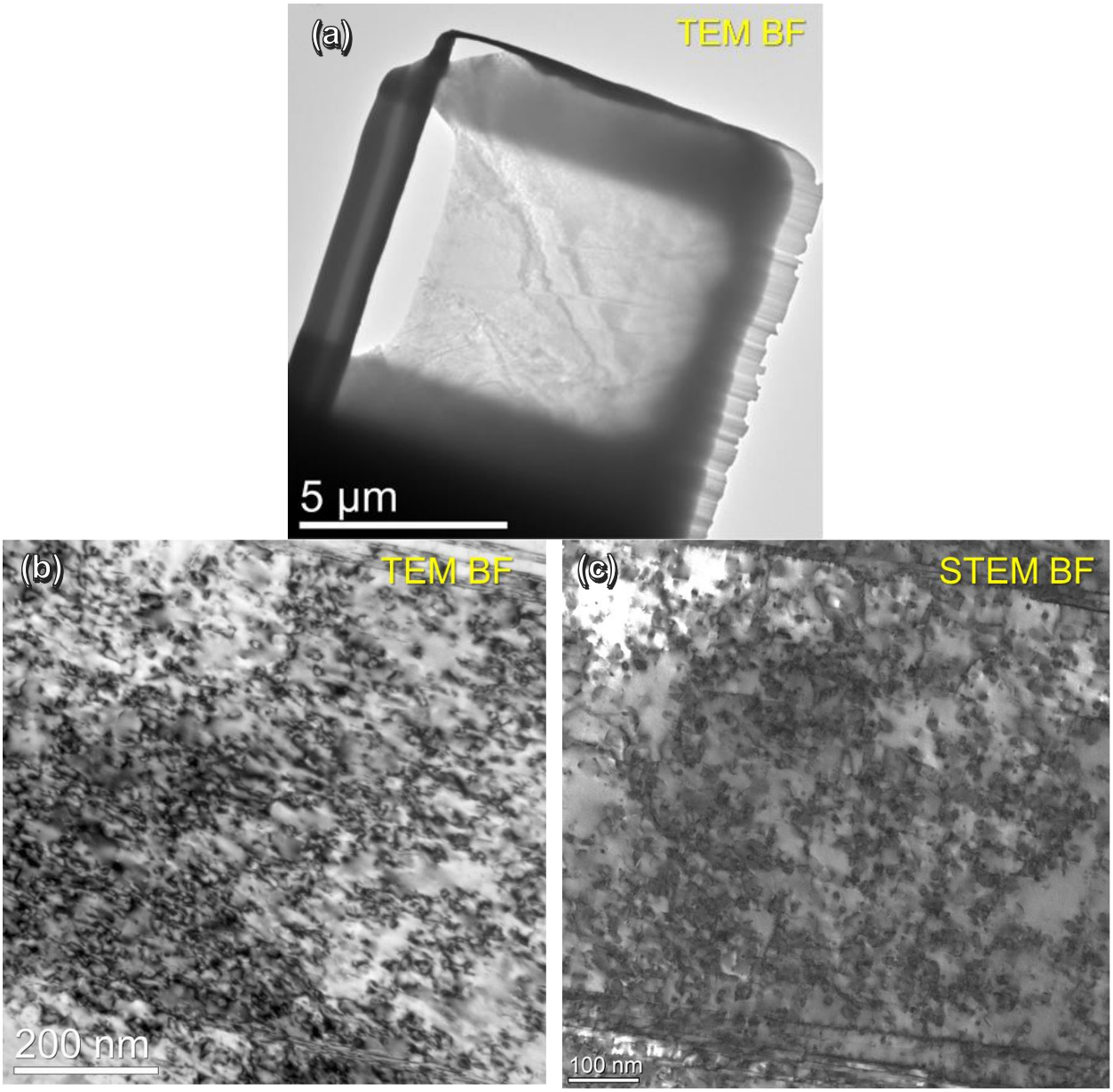

Figure 10. Overview of the FIB lamella with bright field TEM and STEM images below. Cold worked dislocation structure has been restructured into segments that are interacting to form clusters.

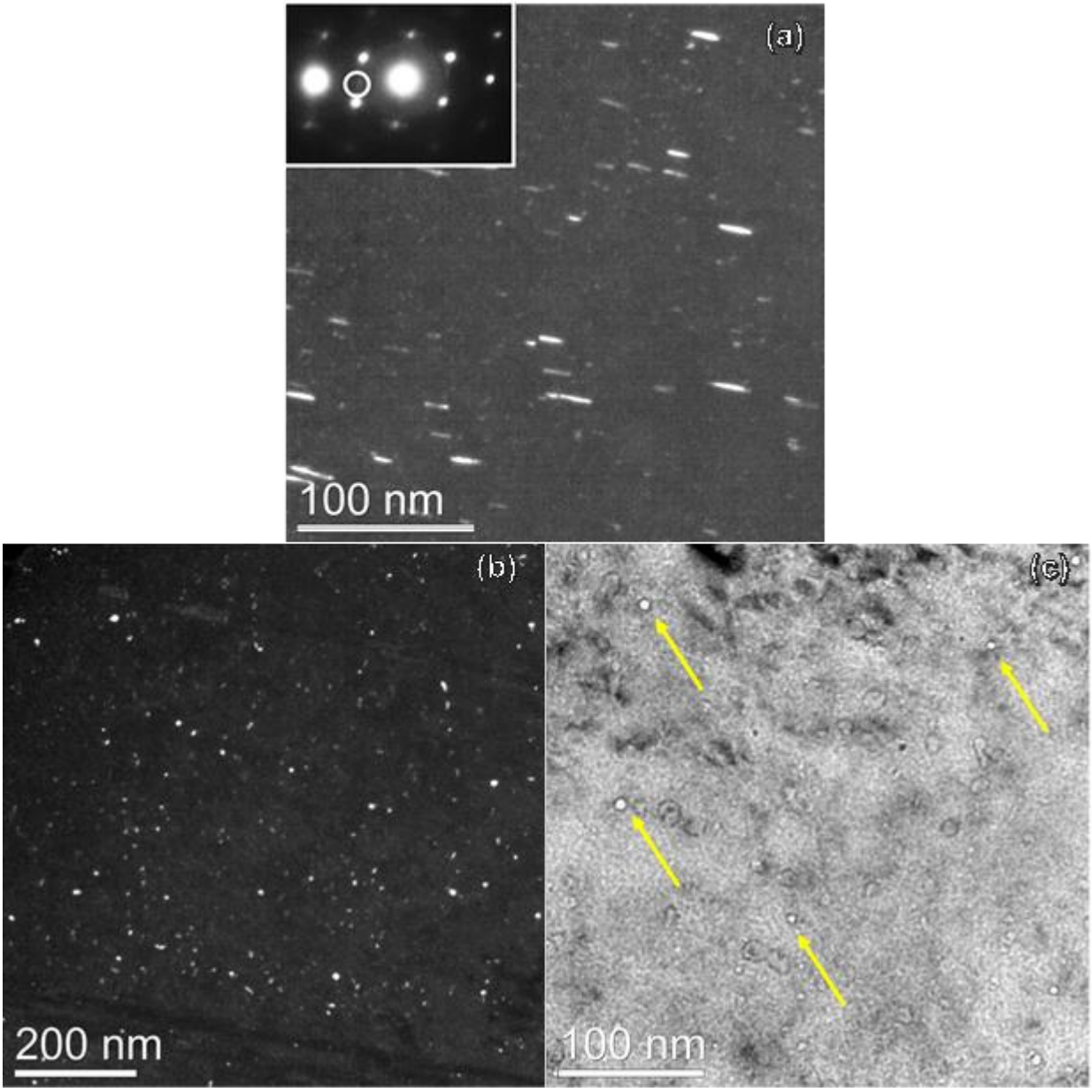

Figure 11. A centered dark field image of edge-on Frank loops is shown in (a), taken using the encircled streak in the diffraction pattern. γ′ precipitates are shown in (b), imaged using a reflection at the 1/2g220 position in the diffraction pattern. A low density of voids are shown in (c), taken by underfocus image in TEM bright field.

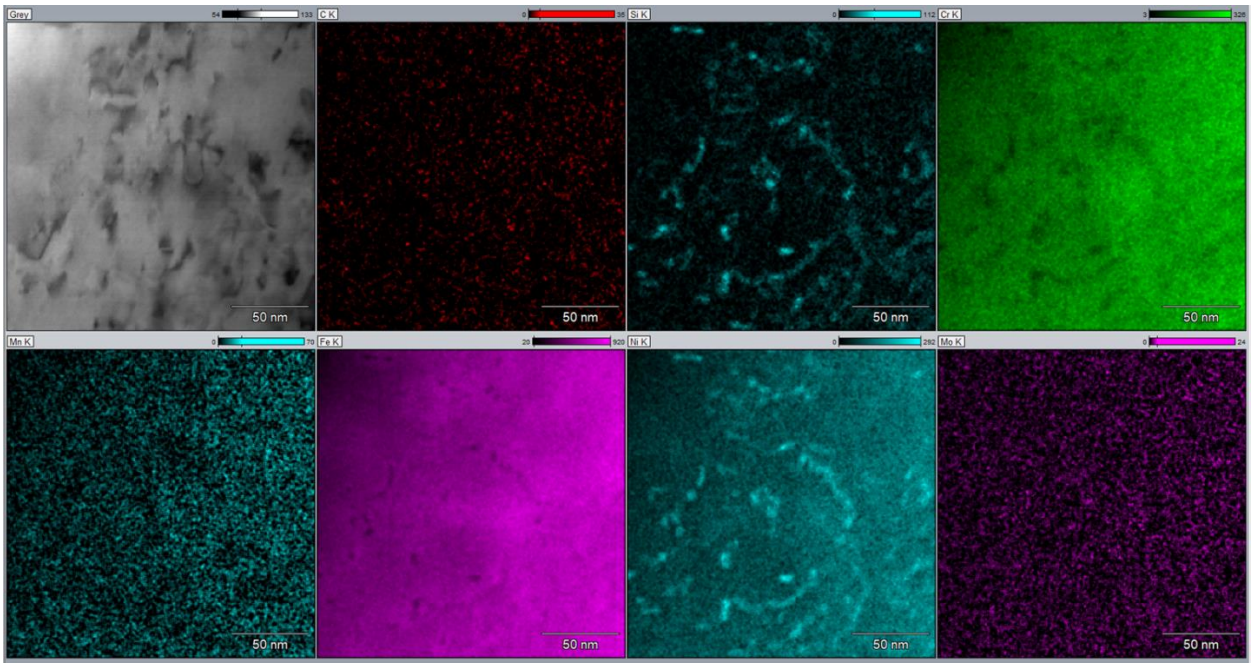

Figure 12. Elemental mapping shows Ni and Si segregation to line dislocations and possible loops. There isn't always a 1-to-1 association between dislocation and Ni/Si, but some loops and dislocations are out of contrast at this tilt. The ratio of Ni/Si is ~3 to 1, suggesting it could be γ′ precipitation on dislocations.

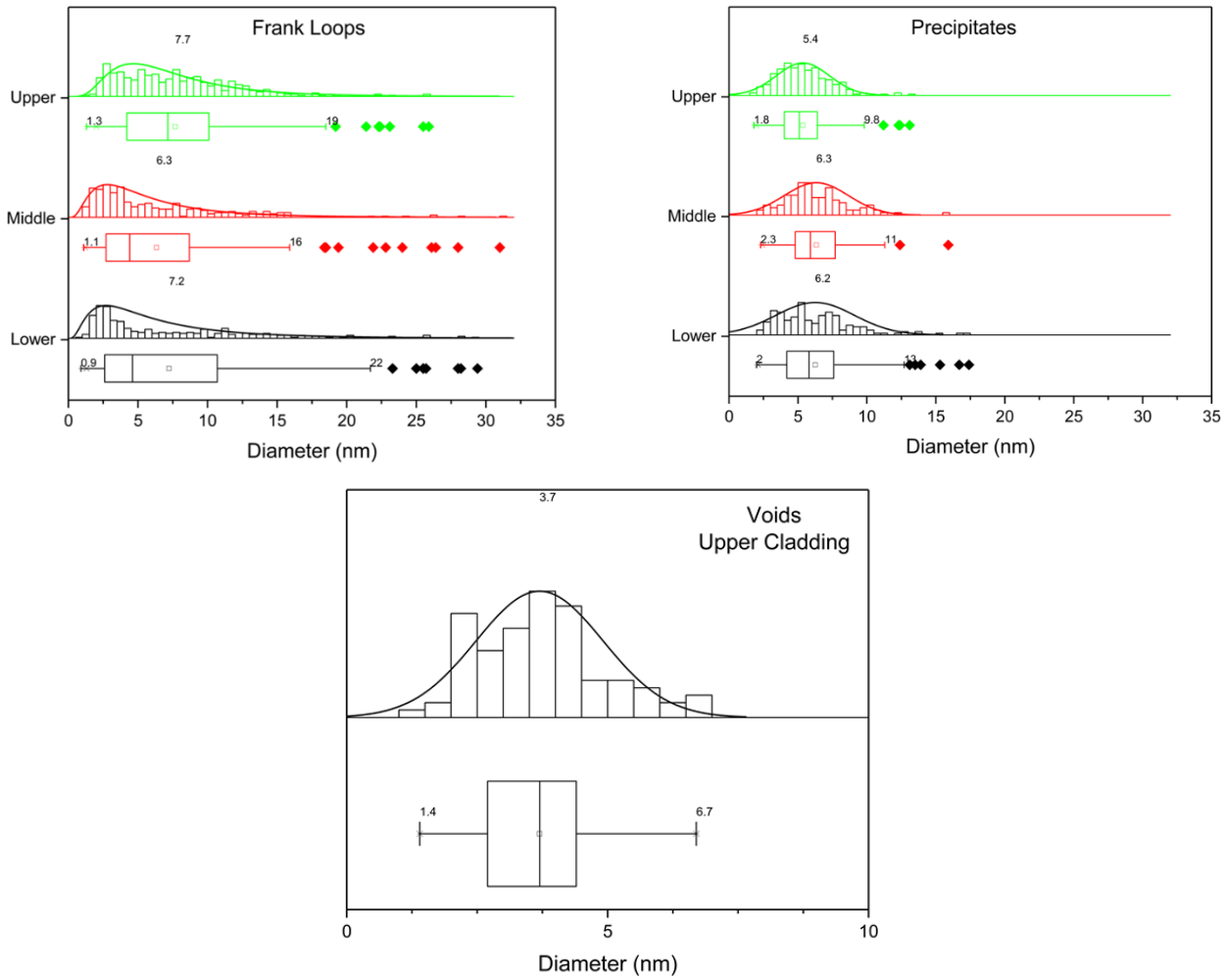

Figure 13. A comparison of the Frank loop, precipitate, and void distributions for each of the three locations in the TPBAR. Note voids were only observed in the upper region of the TPBAR.

Table 3. Density and Average Size of Defects in Irradiated Cladding

Location Along TPBAR	Dose (dpa)	Irradiation Temperature (°C)	Frank Loop Density & Avg. Size	Precipitate Density & Avg. Size	Void or SFT Density & Avg. Size
Upper End	~5.5	320-325°C	5.8 x 10^{22} m^{-3} (7.2 nm)	0.4 x 10^{22} m^{-3} (6.2 nm)	(Voids) 1.0 x 10^{22} m^{-3} (3.7 nm)
Mid Plane	~5.5	315°C	8.6 x 10^{22} m^{-3} (6.3 nm)	0.9 x 10^{22} m^{-3} (6.3 nm)	(SFT) ~1.0 x 10^{22} m^{-3}, (~ 2 nm)
Lower End	~4.7	300°C	4.2 x 10^{22} m^{-3} 7.7 nm	1.2 x 10^{22} m^{-3} 5.4 nm	---------

3.2.3 Midplane Location

Two TEM lamella were taken from the midplane location. One successfully captured a grain boundary in the waterside of the cladding and the other captured inclined grain boundaries from the middle of the cross-section. The dislocation structure exhibits many microstructural similarities with the upper location, but in this case there were no cavities present, only small vacancy-type stacking fault tetrahedra at a lower density. An image of the overall FIB sample is shown in **Figure 14**, plus examples of the relatively intact carbide structure after irradiation. Dislocation loop images using centered dark field and bright field imaging in TEM mode are shown in **Figure 15(a) and (b)** respectively, again showing that many small defects less than 1-2 nm are visible in the dark field image. The bright field image shows small stacking fault tetrahedra are present at this location at ~1 x 10^{22} m^{-3}, approximately 10% of that of the Frank loops. The γ′ precipitates were captured using centered dark field imaging on the reflection at the ½**g**220 position, showing an apparently random distribution of precipitates throughout the grain. In an attempt to investigate the nature of the dislocation loops in the irradiated cladding to determine their nature, HAADF imaging was employed using the aberration corrected STEM probe. This type of work requires a very good sample with minimal bend contours and stress from surrounding features, difficult under the best of conditions in these heavily irradiated microstructures. We were successful in finding one large loop imaged edge-on at the 110 zone axis orientation that revealed the distinct extra-half plane inserted in the lattice which corresponds to a Frank interstitial loop. The images in **Figure 16** show both the raw image of the loop and subsequent images processed using FFT, filtered using an array mask or a spot mask to select the 111 planes. The images in **Figure 16(c) and (d)** show a close-up of the inserted half plane, and the dis-registry this causes in the lattice, leading to strain at the tip of the loop (red encircled region). Additional attempts didn't reveal any of the smaller defects that may be vacancy or interstitial defects, but this was hindered due to build-up of hydrocarbons on the surface.

One of the surprising discoveries was the extensive RIS that leads to Ni and Si enrichment, accompanied by extreme Cr depletion, on the sensitized grain boundaries. As shown in **Figure 17**, two sets of elemental maps show the extent of this RIS, both in the matrix and on the grain boundary with a large carbide captured in a thin region of the flash electropolished foil. EDS analysis of the precipitates in the matrix reveal the same ratio of Ni/Si as observed in the upper region, confirming their identity as γ′. The greatest surprise, however, involved the degree of RIS on the grain boundary proper and around the interface of the carbide, which should be evident in the maps. Line profiles (**Figure 18**) extracted from the high resolution, high count elemental maps confirmed this RIS, demonstrating Ni enrichments up to ~40 wt% and Si levels up to ~12%, with the Cr depleted to ~8 wt% and the Fe depleted down to ~38 wt%. The profile width has changed from a thermally sensitized width of ±250 nm to a prototypical RIS profile width of ±10 nm, with most of the enrichment occurring in a narrower width of ±5 nm. These levels of enrichment and depletion are higher than found in any of irradiated commercial 316SS, and for the moment, can only be assumed to be a direct consequence of the moderately sensitized state when placed into service [ref?]. One source of the high levels of RIS may be the γ′ precipitation observed on an inclined grain boundary in a FIB sample extracted from the lower TPBAR position, described in the next section.

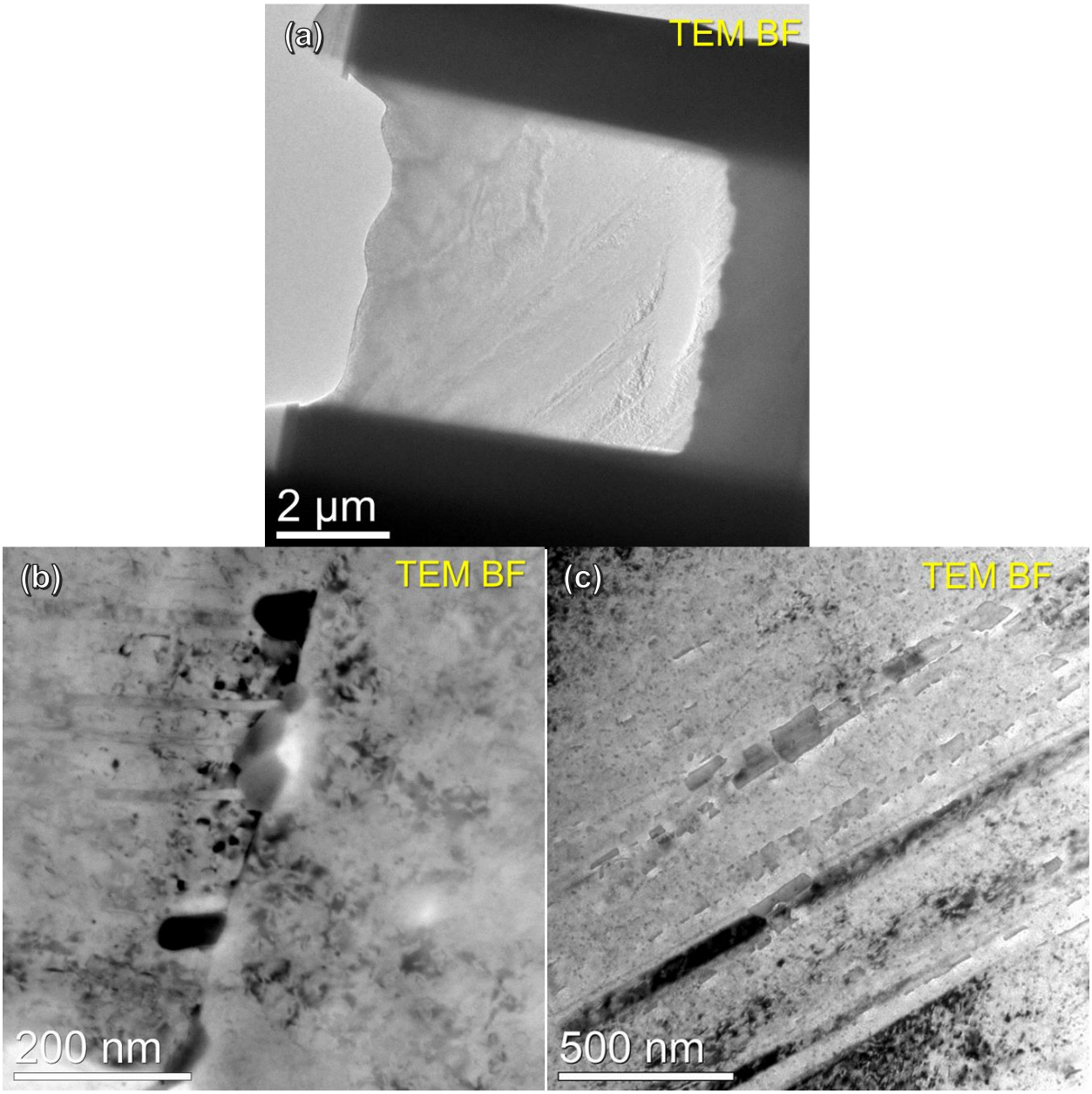

Figure 14. The TEM bright field image in (a) shows an overview of the TEM lamella. Examples of the carbides still present after irradiation are shown in (b) and (c), the latter of which are on a inclined twin boundaries within the foil.

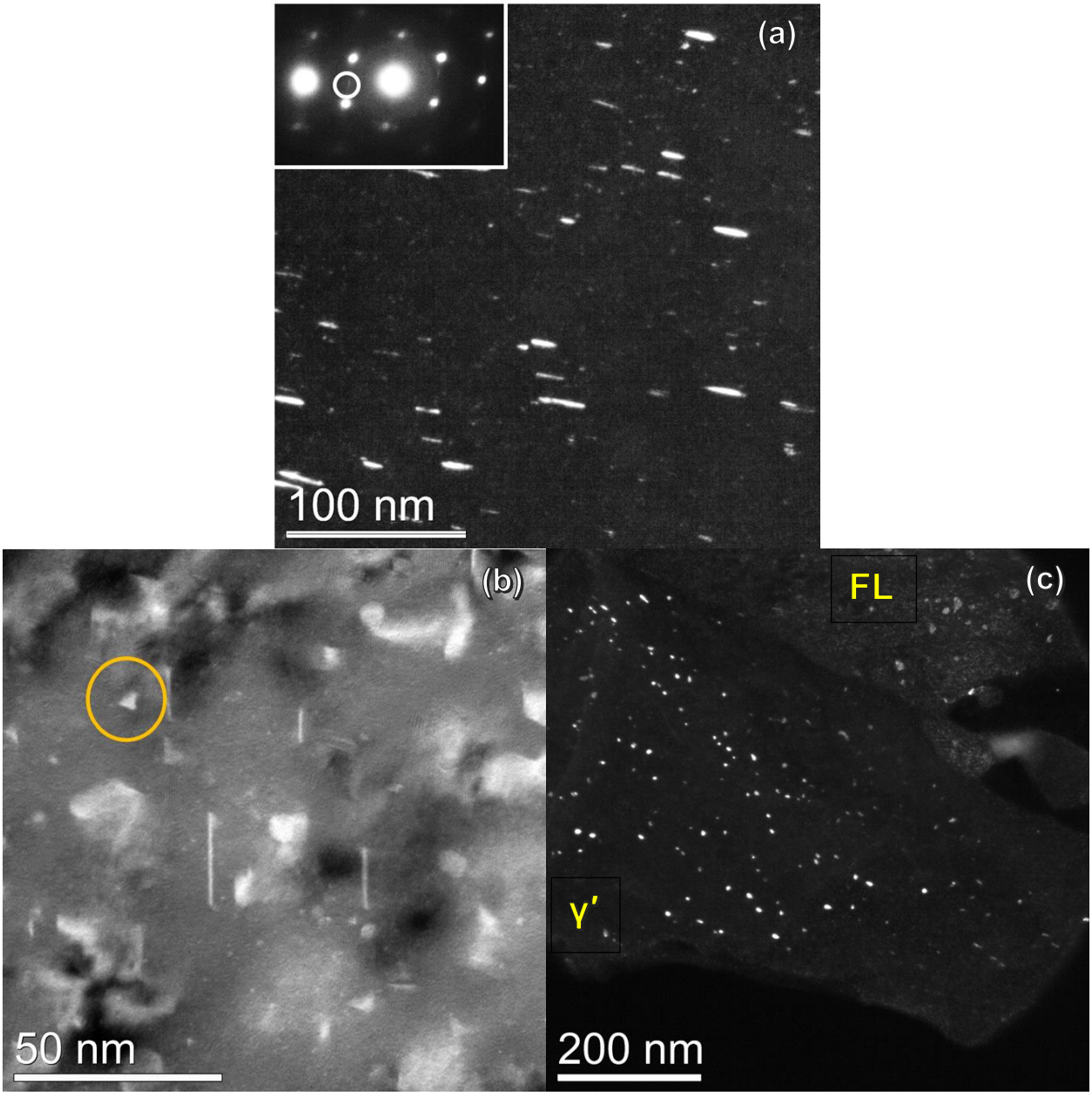

Figure 15. In the middle position, Frank loops, stacking fault tetrahedra and γ′ precipitation are all present, with no indication of cavities. Edge-on loops are shown in CDF in (a), with both the edge-on loops and small SFT visible in the TEM bright field image in (b). In (c) CDF imaging was used to show the distribution of γ′ precipitates in the bottom grain. In the upper RH corner of are CDF images of inclined Frank loops (FL).

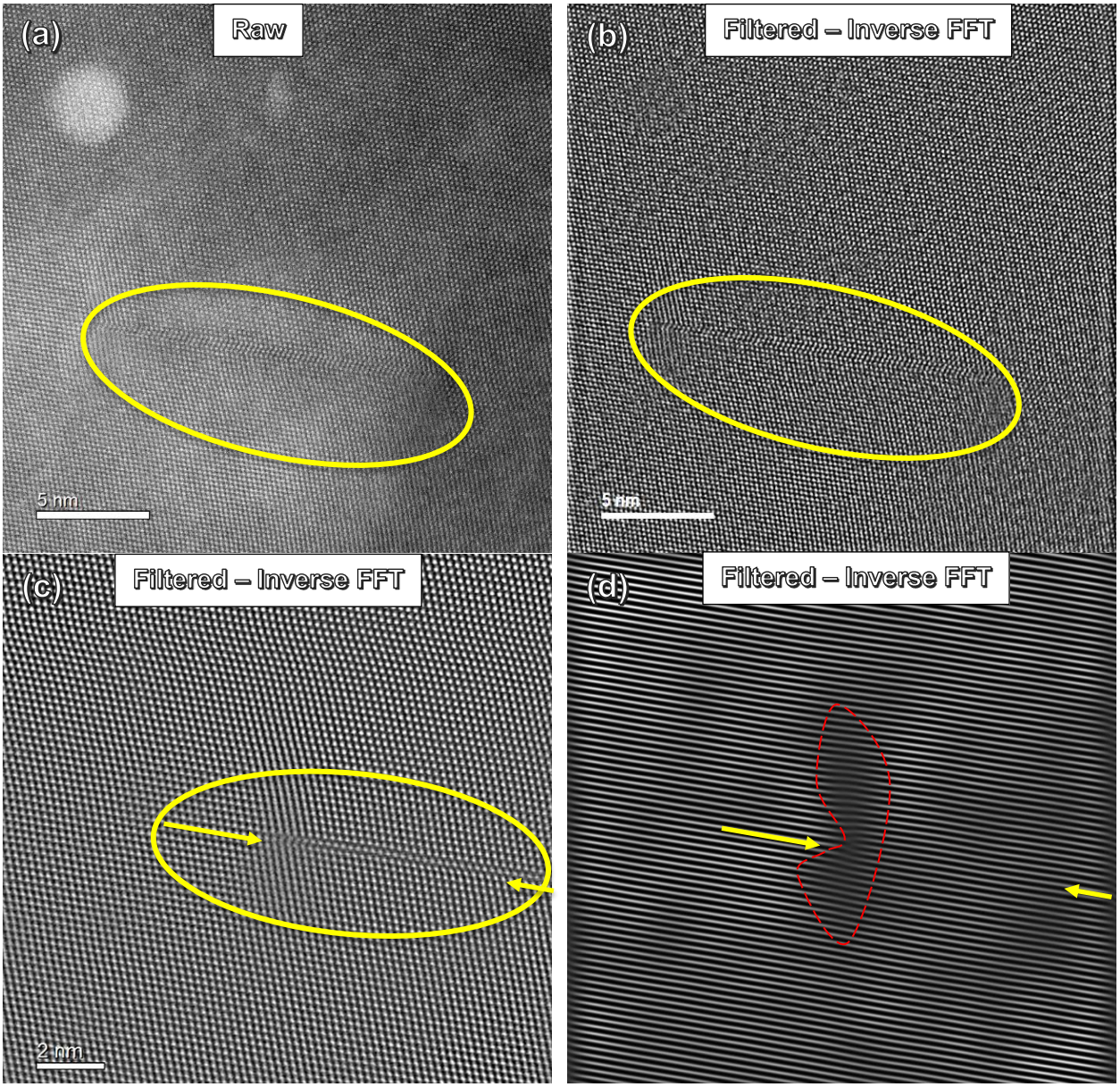

Figure 16. Lattice images taken in high angle annular dark field show an edge-on Frank loop (inside the yellow ellipse) ~15 nm in diameter. (a) is the raw image, (b) has been filtered using an inverse FFT of the image in (a) after applying an array mask on the power spectra from the image. The image in (c) is a close-up of one end of the loop, with the yellow arrows pointing to the inserted half-plane. The image in (d) is the same loop, but filtered using a spot mask within Digital Micrograph. The dark regions enclosed by the red dotted line are regions of lattice dis-registry due to strain at the end of the loop.

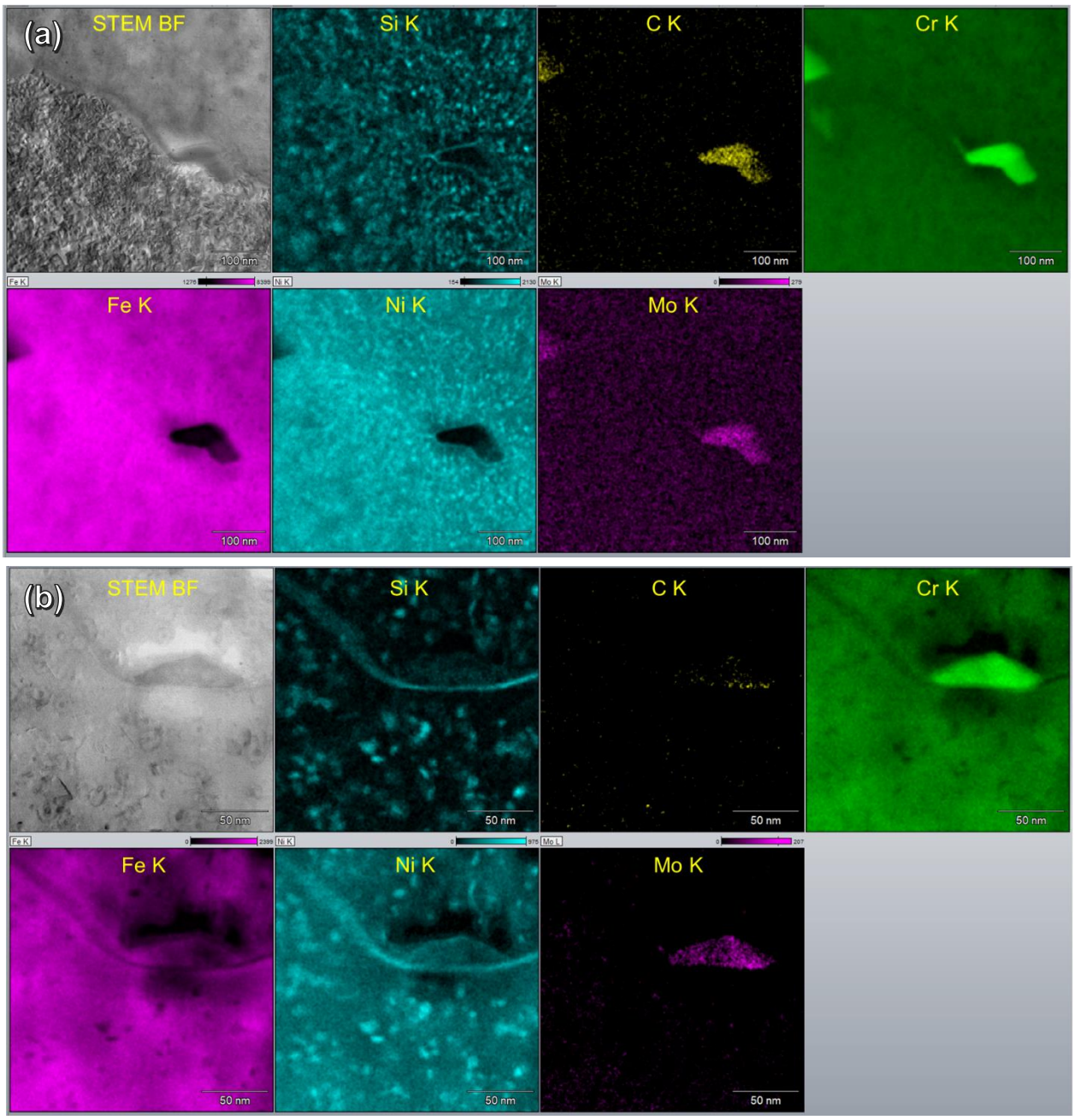

Figure 17. Two sets of elemental maps are shown highlighting the extreme degree of RIS of Ni and Si to the grain boundary, carbide interface, and nearby matrix regions. Up to 40% Ni and 17% Si, accompanied by a depletion of Cr down to 8wt%, is present in this condition. The high levels of Ni and Si on the boundary may be evidence of γ′ precipitation, not just solute segregation.

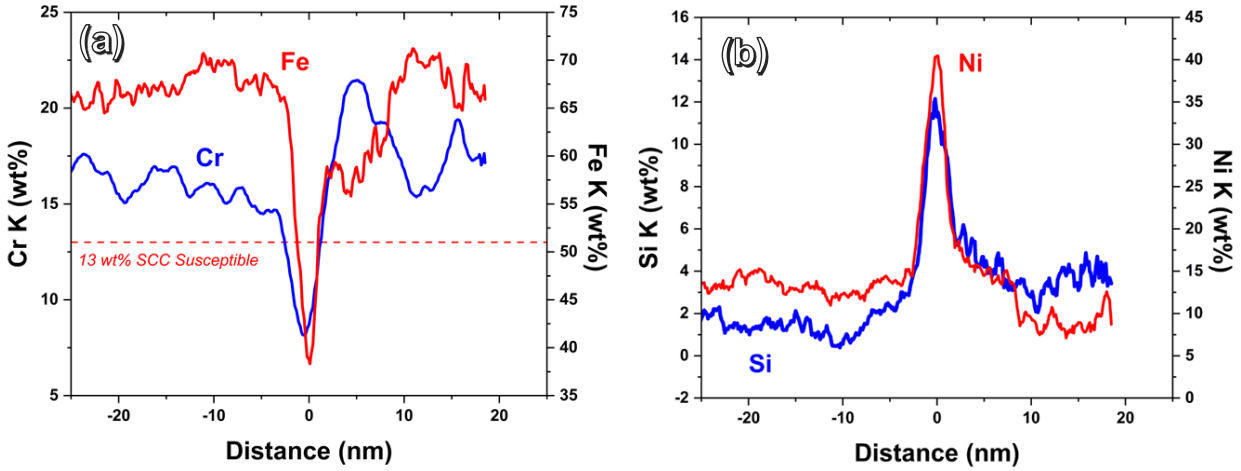

Figure 18. RIS profiles show the extreme levels of Ni and Si enrichment and the accompanying Cr and Fe depletion. The Cr levels are near 8 wt%, whereas the Ni is at 40% and Si at 12%, close to the 3 to 1 ratio of γ′ precipitates. These levels of Si and Ni are higher than any reported in the literature or based on the author's experience.

3.2.4 Lower Location of Cycle 13 TPBAR

At the lower location, the loop and dislocation clustering visible at the midplane and upper location are present also. **Figure 19** shows examples of the clustered defect distribution of line dislocations segments and dislocation loops. This clustering of loops and dislocations into a cellular wall type structure with defect free regions in-between the walls is not a common microstructural feature based on the authors experience. In looking back through the results obtained in prior work on BOR60 irradiations of model and commercial alloys, and core components such as PWR baffle bolts, PWR Flux thimble tubes, BWR core shrouds, the line dislocation and Frank loop distribution has always been found to be uniform over large areas. The TEM dark field image in **Figure 20(a)** show the Frank loops imaged edge-on, with smaller bright dots in the background that may be loops or SFT. The remaining images show inclined Frank loops in the vicinity of a grain boundary, with γ′ decorating line dislocations in the grain boundary and in the nearby matrix, along with other γ′ precipitates formed in the matrix at random. It is not clear if the isolated precipitates are forming on loops, this association hasn't been proven directly in this work.

The elemental maps in **Figure 21** show once again that Ni and Si have segregated to these clusters of loops and line dislocations. The Ni and Si are associated with the line dislocations, but the discrete, isolated precipitates are not necessarily associated directly with individual loops. **Figure 22** presents a multivariate statistical analysis of the chemical segregation present in the previous image, and the resulting phase map produced by the Pathfinder software package used to obtain this data indicates that both the Ni-Si regions on the line dislocations and in the discrete particles have the same composition, with a γ′ Ni/Si ratio of 3 to 1.

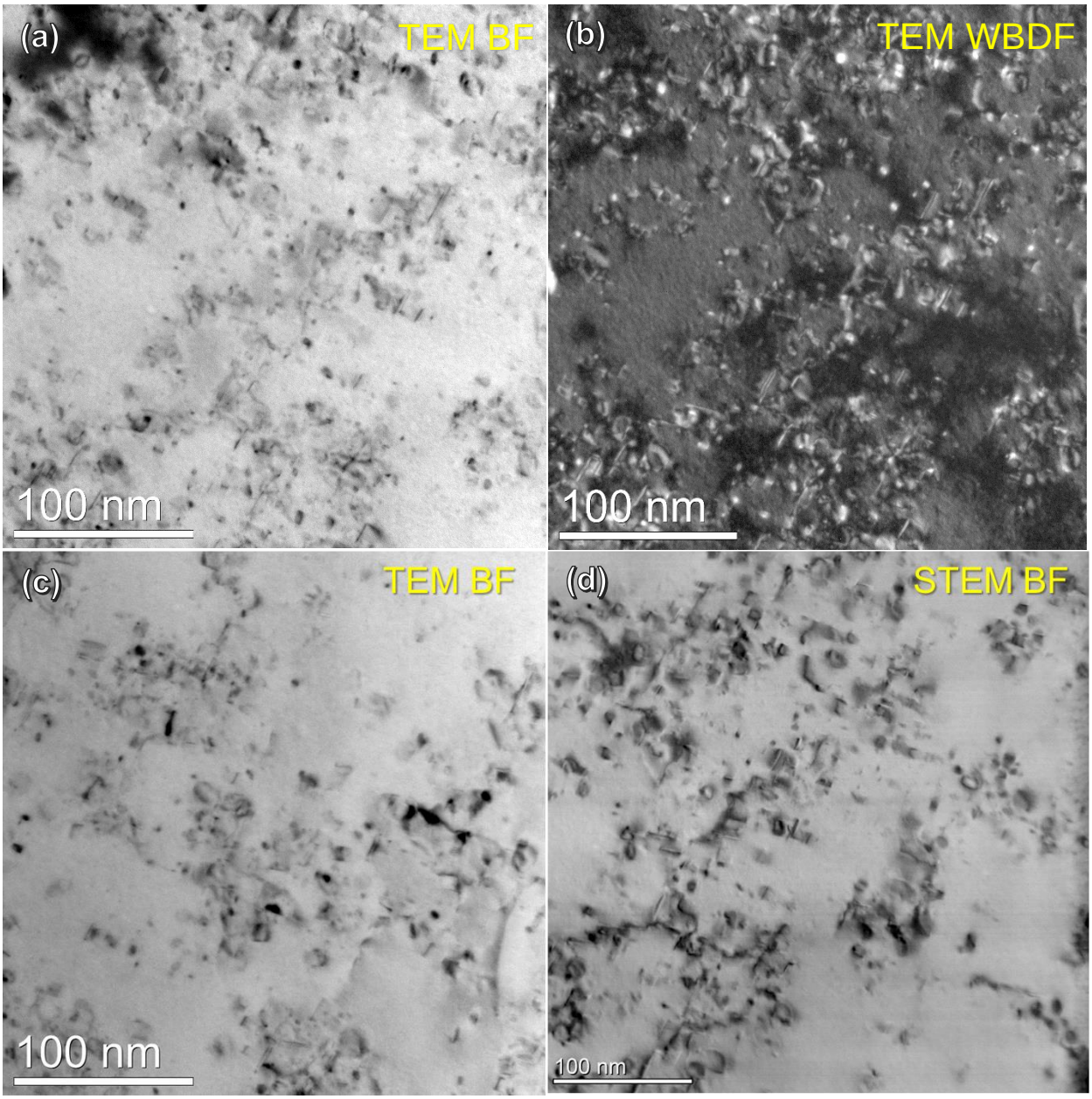

Figure 19. The TEM bright field image in (a) and centered dark field image in (b) show the clustering of the loops and line dislocations, with no evidence of SFT in this condition. The bright field images in (c) and (d) show additional examples of the inhomogeneous distribution of loops and line dislocations.

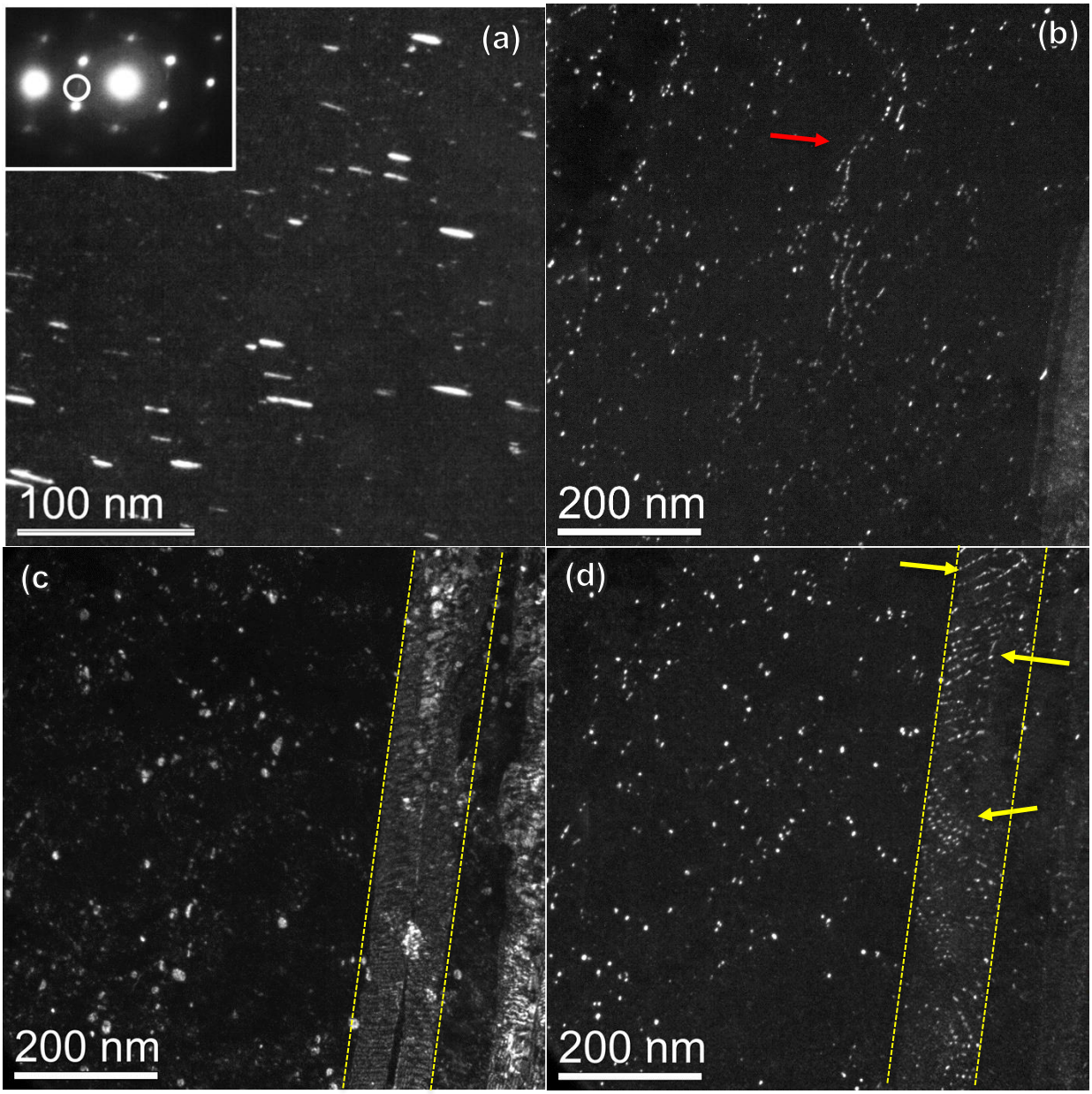

Figure 20. Centered dark field images are shown in (a) for edge-on loops Frank loops and (b) γ′ that has formed on dislocations within the matrix near a grain boundary. The centered dark field image in (c) shows inclined Frank loops in the same area as in (d), which shows γ′ precipitation on grain boundary dislocations (yellow arrows and dashed lines) and in the matrix.

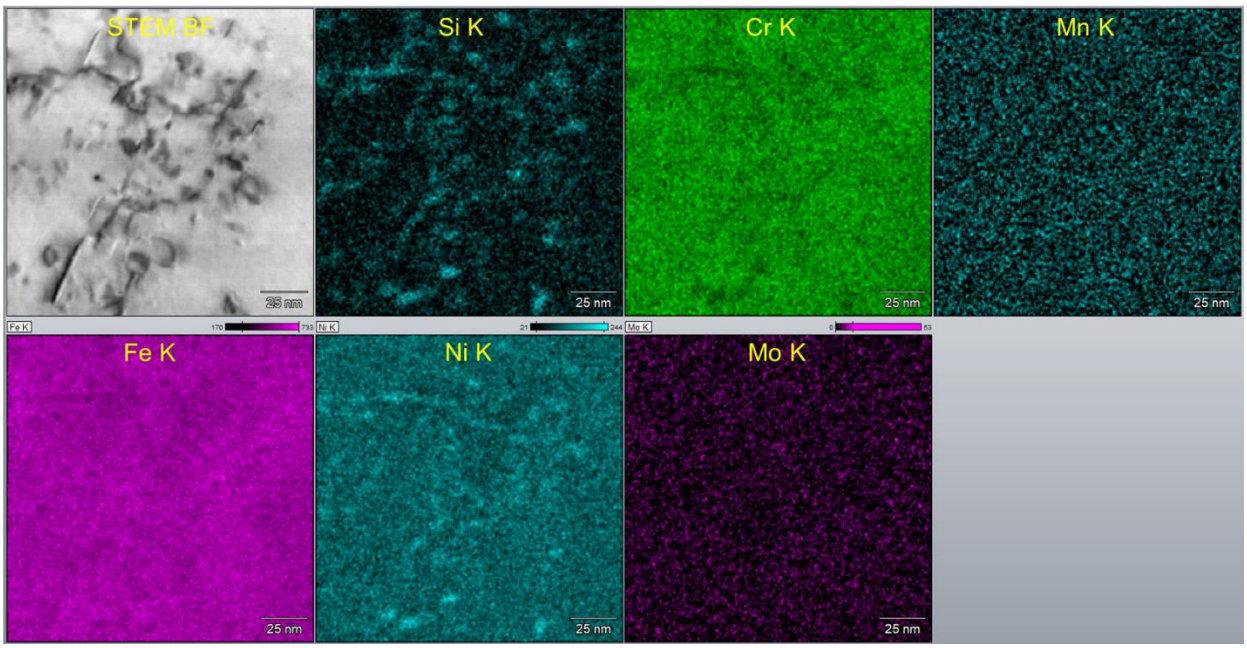

Figure 21. This elemental map shows a region of clustered line dislocations and loops with significant Ni and Si enrichment, offset by Cr and Fe depletion.

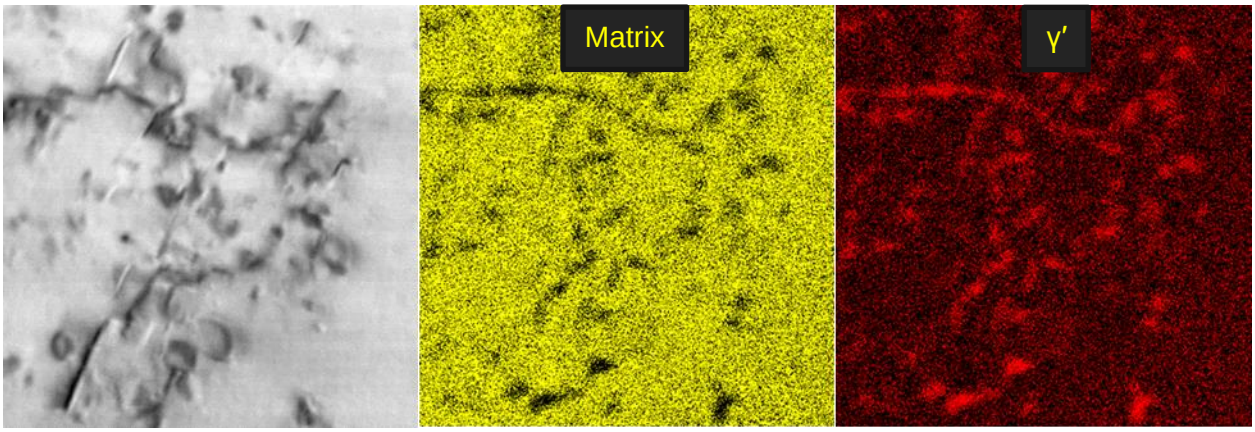

Figure 22. From the maps in the previous figure, phase maps derived from the multivariate statistical analysis module within the software show that the Ni-Si rich regions have approximately the same composition with a Ni to Si ratio of ~3:1.

4.0 Summary and Conclusions

Optical, SEM and TEM analysis confirmed the presence of moderate sensitization in the 20% cold worked 316SS after the iron aluminide coating was applied, as demonstrated by the semi-continuous distribution of $M_{23}C_6$ carbides on the grain boundaries and twins, and by the Cr-depletion measured in the sensitized material. The Cr depletion occurs on the grain boundaries between the closely spaced carbides, and at the interface between the carbides and matrix. Cr depletion varied locally along the grain boundaries, in many cases showing levels down to 15 wt%, but a few isolated regions had depletions levels down to 12.5 wt%. The depletion of Cr around the periphery of the carbides was identical to what was observed at the grain boundaries. Bruemmer et al. indicated that austenitic stainless steels become increasingly susceptible to stress corrosion cracking as the Cr levels depleted to less than 12.5 to 13.5%. These results were based on EPR (electrochemical potentiokinetic reactivation) testing of various thermally sensitized 304 and 316 stainless steels and correlated with Cr depletion profiles measured in a STEM with a probe size of 10 nm. The microstructure of the cold worked cladding was heavily twinned, with a dislocation density near the limit of what can be easily separated by TEM methods (~10^{15} m^{-2}).

Optical and SEM images taken from the weld heat affected zone where an end cap plug was welded to the cladding revealed that recrystallization occurred, which in turn resolutionized the carbides and removed the cold work in regions close the weld. There is a gradient in this recrystallization response as you move further away from the weld, which tails off near the edge of the HAZ and into the base metal. A TEM sample extracted from a recrystallized region in the HAZ revealed no carbides and very low dislocation density, confirming the optical and SEM imaging. Not only was the Cr depletion completely removed, it was replaced by a slight enrichment of Cr and Mo. This latter enrichment is known as a thermal nonequilibrium segregation (TNES), and has been found to occur in mill annealed stainless steels. It was found to have positive effect in delaying the onset of Cr depletion during subsequent irradiation, but this benefit occurred only when much higher levels of Cr and particularly Mo enrichment were produced by mill annealing, levels of which were higher than seen in this recrystallized region.

Irradiation of the coated cladding produced some surprising changes to the microstructure when compared to results obtained for other light water and fast reactor irradiated 304 and 316SS. The first observation was the restructuring of the cold worked dislocation structure into a mix of line dislocation segments and loops, which clustered together to form an ill-defined, pseudo-cellular structure with the interior regions relatively free of defects. In other neutron irradiated stainless steels, the cold worked dislocation either remained relatively unaffected (fast reactor irradiations – higher displacement rate at same temperature), or was completely removed and replaced with a much lower density of line dislocation segments (Flux Thimble tube – much lower displacement rate, same irradiation temperature). In addition to clustering defects, the present work on the coated cladding revealed that neutron irradiation produced a high degree of RIS of Ni and Si to the line dislocations segments, and formed precipitates in the matrix and on grain boundaries. The Ni/Si ratios measured on the line dislocations, grain boundaries, and on discrete precipitates proved to be similar, matching that of the γ′ Ni_3Si phase. This was confirmed by dark field imaging using a precipitate reflection in the diffraction pattern that corresponds to γ′. In the lower end sample, direct evidence of γ′ precipitation was observed on both matrix dislocations and dislocations within a grain boundary that happened to be inclined in the foil, thereby allowing a direct observation of the precipitates using dark field imaging. The RIS of Ni and Si to the grain boundaries also depleted the Cr from the boundaries. The broad (±250 nm) Cr depletion profile produced by sensitization was effectively removed, and replaced by a much narrower and deeply

depleted Cr profile (±10 nm) with minimum Cr levels of 8 wt% or more. As the Cr depleted further and the sensitization profile was altered to a more typical RIS profile, this led to enrichment of the Ni to levels of ~40 wt% and the Si to ~12 wt%, levels not observed in any other LWR irradiated stainless steel. This level of Cr depletion places the coated 316SS cladding well into the susceptible range, made worse by the presence of high levels of Si that some researchers believe hinders the passivation of a crack once it forms and begins to propagate [ref?]. It appears that the presence of a sensitized grain boundary chemistry makes the coated cladding even more susceptible to Cr depletion and Ni/Si enrichment. The reasons for this are not yet know, but was speculated by Okada et al [5] to be related to the lack of free carbon in the grain boundary regions, which may increase the defect mobility that controls RIS. The Si levels in this material were not out of bounds, so the results bear further study to understand why the kinetics of RIS are so high to allow such a high degree of γ′ throughout the grains and interfaces.

With respect to the susceptibility to stress corrosion cracking and irradiation-assisted stress corrosion cracking of this coated cladding, it is worth noting that the over 6500 TPBARs have been irradiated without any known incidences of cracking. This is likely due to the combination of the low corrosion potential in the PWR water and to a low stress in the cladding. It is assumed by the authors that as the TPBARs are removed from the reactor and placed in a spent fuel pool, the internal gas pressure from the helium will decrease quickly as the temperature decreases. With respect to the susceptibility to stress corrosion cracking and irradiation-assisted stress corrosion cracking of this coated cladding, it is worth noting that the over 6500 TPBARs have been irradiated without any known incidences of cracking. This is likely due to the combination of the low corrosion potential in the PWR water and to a low stress in the cladding. With respect to stresses, it is assumed by the authors that as the TPBARs are removed from reactor and placed in a spent fuel pool, the internal gas pressure from the helium will decrease quickly as the temperature decreases, hence removing the stress during storage in the pool. During service, a couple of potential issues that might warrant investigation are related to void swelling and residual stresses from the welding of the end plug caps. If there are regions within the assembly with where the irradiation temperature and dose are high enough to promote void swelling, there might be unexpected stresses due to unrelieved volume expansion if the swelling region is sufficiently constrained. The HAZ of the end plug has a much different microstructure than the rest of the TPBAR cladding, so how it evolves with respect to swelling may be different than the more highly cold worked and sensitized cladding. Finally, residual stresses around the HAZs in welded core components have been areas that have seen cracking failures in LWRs, so it may be worthwhile to perform PIE on those regions if the irradiation temperature and dose are high enough.

The abnormal microstructures observed in this irradiated cladding bears further analysis, particularly comparing to other parts of the TPBAR such as the end plug assembly that might have similar overall chemistry, but a much different, unsensitized grain structure. If we can find regions of comparable dose and temperature to the cold worked coated cladding, then we might be able to make an interesting comparison to see how the removal of cold work and the Cr depletion/carbides affects the microstructural evolution.

5.0 References

1. Schemer-Kohrn, A., Toloczko, M., Zhu, Y., Wang, J., & Edwards, D. (2019). Removal of FIB Damage using Flash Electropolishing for Artifact-free TEM Foils. *Microscopy and Microanalysis, 25*(S2), 1606-1607. doi:10.1017/S1431927619008766
2. Edwards, D.J., Simonen, E.P., & Bruemmer, S.M. (Apr 2003). Evolution of fine-scale defects in stainless steels neutron-irradiated at 275 deg. Journal of Nuclear Materials, 317(1), 13-31. doi:10.1016/S0022-3115(03)00002-3
3. Bruemmer, S. M., et al. (1988). "Sensitization Development in Austenitic Stainless Steel: Correlation between STEM-EDS and EPR Measurements." CORROSION **44**(6): 328-333.
4. Bruemmer, S. (2004). Linking Grain Boundary Structure and Composition to Intergranular Stress Corrosion Cracking of Austenitic Stainless Steels. *MRS Proceedings, 819*, N2.2. doi:10.1557/PROC-819-N2.2
5. Okada, O; Nakata, K. and Kasahara, S.; (November 1998) “Effects of Thermal Sensitization on Radiation-Induced Segregation in Type 304 Stainless Steel Irradiated with He-Ions.” Journal of Nuclear Materials, 265, 232-239.

Pacific Northwest National Laboratory

902 Battelle Boulevard
P.O. Box 999
Richland, WA 99354
1-888-375-PNNL (7665)

www.pnnl.gov